Research Article Vol. 30, No. 23 / 7 Nov 2022 / *Optics Express* 41473

Optics EXPRESS

Improving the precision of parallel registration by incorporating a priori information

NIKOLAUS BERLAKOVICH,* MARTIN FUERST, ERNST CSENCSICS, AND GEORG SCHITTER

Christian Doppler Laboratory for Precision Engineering for Automated In-Line Metrology, Automation and Control Institute (ACIN), TU Wien, 1040 Vienna, Austria
*berlakovich@acin.tuwien.ac.at

Abstract: This paper presents an algorithm for the precise registration of optical wavefronts. A wavefront exceeding the spatial or dynamic measurement range of a wavefront sensor, e.g. a Shack-Hartmann sensor, can be measured in multiple sub-measurements, each providing a segment of the wavefront. Sensor misalignment during the measurements results in the demand for registration algorithms to precisely reconstruct the entire wavefront from the segments. The proposed algorithm registers the segments in parallel and incorporates a priori information about the uncertainty of the sensor misalignment obtaining high-quality registration. A simulative analysis of the algorithm with respect to sensor misalignment and measurement errors is presented together with an application of the algorithm to a measured divergent wavefront. In the scope of the analysis, the algorithm is compared to state-of-the-art registration algorithms, such as the iterative closest point (ICP) algorithm, where an improvement of the registration performance by a factor of 3 is obtained. Results show that the algorithm is able to reconstruct a divergent and a freeform wavefront with an RMS registration error of a few tens of nanometers with a standard deviation of 80 μm and 2.4 $mrad$.

1. Introduction

The performance of an optical system corresponds to the conversion of an optical wavefront, passing through the system, into a desired wavefront. Using a wavefront sensor the optical wavefront is measured enabling the evaluation of the performance of the optical system. Among several types of wavefront sensors [1] the Shack-Hartman sensor (SHS) is attractive, as it can measure the wavefront directly without a reference. In addition, the SHS is less sensitive to vibrations as compared to other wavefront sensors [2]. For the measurement of highly divergent wavefronts or wavefronts with large diameters additional supporting optics, like null optics or shrinking optics [3], are typically necessary to provide a measurable wavefront within the dynamic range and the aperture size of the sensor. A drawback of supporting optics is that they cause additional errors in the wavefront [4]. Moreover, for complex shaped wavefronts it might be challenging to assemble the appropriate supporting optics [5]. In [6–8] a measurement system is proposed where no supporting optics are needed to measure highly divergent wavefronts as well as large wavefronts. In particular, the wavefront is directly measured at multiple locations using an SHS in combination with a positioning system. Each individual measurement provides a segment of the wavefront and using the positioning data of the SHS, the segments can be registered to obtain the entire wavefront. The task of registering the segments can be a challenge due to errors in the positioning data, resulting in the need for registration algorithms to attain small registration errors. These algorithms find the correct position and alignment of the segments by minimizing the overlap mismatch between the segments. In literature different kinds of algorithms are found for the registration of segments of an optical wavefront, e.g. the iterative closest point

#469299 https://doi.org/10.1364/OE.469299
Journal © 2022 Received 30 Jun 2022; revised 26 Sep 2022; accepted 27 Sep 2022; published 27 Oct 2022

(ICP) algorithm [9]. Registration algorithms based on the least squares method are proposed to minimize the overlap mismatch [10,11]. Algorithms enabling parallel registration are developed where the overlap mismatch between all segments is simultaneously minimized [12,13]. In [14,15] parallel registration algorithms are proposed that allow for the precise reconstruction of freeform wavefronts, i.e. wavefronts with complex shapes generated by freeform optics [16]. This is in particular achieved by minimizing the overlap mismatch with respect to the position, the alignment and the phase of the segments. None of the proposed registration algorithms, however, can incorporate a priori information about the errors in the positioning data, such as underlying statistical properties, to improve the accuracy of the registration. A derivation of the statistical properties of the positioning errors may be possible [17] along with an experimental characterisation.

The contribution of this paper is the development and evaluation of a registration algorithm that incorporates a-prior information about the errors in the positioning data to increase the registration performance. In particular, the standard deviation of the errors is used to constrain the segments to relevant domains obtaining an improved quality of the registration. The algorithm registers the segments in parallel and is able to reconstruct freeform wavefronts with high precision. Section 2. introduces the algorithm and discusses the mathematics. Section 3. presents a simulative analysis of the algorithm. Section 4. presents an application of the algorithm to a measured divergent wavefront and Section 5. concludes the paper.

2. Algorithm description

2.1. Wavefront measurement concept

The SHS is mounted on a positioning system to enable scans of complex and large wavefronts with a diameter 14 times larger than the diameter of the aperture of the sensor [7,8]. During scanning, segments of the wavefront are measured at different locations of the wavefront depicted in Fig. 1. In an individual measurement of the SHS, the gradients of the incident wavefront segment are determined at grid points [18]. A point cloud is then reconstructed from the gradients, where each point of the point cloud corresponds to a point of the segment in the local coordinate system of the sensor. For the reconstruction of the point cloud, zonal as well as modal reconstruction algorithms [19,20] can be used where zonal reconstruction algorithms are preferred as they better preserve local variations of the segment [21]. For segments containing huge dynamics, the phase distribution of the optical field over the sensor aperture is reconstructed from the gradients [14]. From the phase distribution the wavefront is then easily determined, as it corresponds to the surface of a specific phase. Uncertainties in the positioning system cause errors in the positioning data which result in an overlap mismatch between the segments when they are combined to reconstruct the entire wavefront. Minimizing the overlap mismatch allows for a precise registration of the segments and reconstruction of the entire wavefront. For this, the segments are rigid body transformed, i.e. translated and rotated with respect to the three spatial dimensions, as well as propagated as illustrated in Fig. 1. The propagation is needed to minimize the overlap mismatch with respect to the phase difference between the segments.

2.2. Parallel registration algorithm incorporating a priori information

From the measurement data each wavefront segment is reconstructed as a point cloud represented in the local coordinate system of the sensor at the corresponding measurement position. To reconstruct the entire wavefront the point clouds have to be appropriately transformed into the global frame (FG). A rough estimate of this transformation is given by $\mathbf{T}_{0i} \in \mathbb{R}^3$, $\mathbf{R}_{0i} \in \mathbb{R}^{3\times 3}$ and $S_{0i} \in \mathbb{R}$ for each segment $i = 1..U$, where $\mathbf{T}_{0i}$ and $\mathbf{R}_{0i}$ correspond to the nominal position and alignment of the sensor during the measurement of the respective segment. The transformation

Published version of the article: Nikolaus Berlakovich, Martin Fuerst, Ernst Csencsics, and Georg Schitter, "Improving the precision of parallel registration by incorporating a priori information," *Optics Express* Vol. 30, Issue 23, pp. 41473-41491, 2022. DOI: 10.1364/OE.469299

Optics EXPRESS

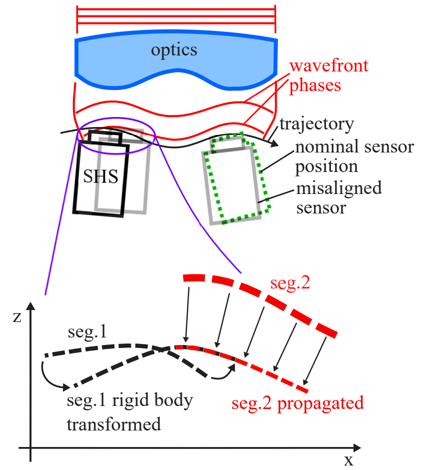

Fig. 1. The SHS scans the wavefront measuring different segments of the wavefront. Uncertainties in the sensor positioning cause an overlap mismatch between the segments. The segments get registered by rigid body transformation and propagation.

of a point ($\mathbf{x}_{0j}^{\{i\}}$) from the local coordinate system of measurement i into FG is then given by

$$\mathbf{x}_{0j} = \mathbf{R}_{0i}\,(\mathbf{x}_{0j}^{\{i\}} + \mathbf{n}_{0j}^{\{i\}}\,S_{0i}) + \mathbf{T}_{0i} \in P_{0i}, \tag{1}$$

where $\mathbf{n}_{0j}^{\{i\}}$ is the unit normal vector of the segment at the point and P_{0i} denotes the transformed point cloud in FG. The upper index in curly brackets in Eq. (1) indicates the local coordinate system in which the objects are represented. While $\mathbf{T}_{0i}$ and $\mathbf{R}_{0i}$ define a rigid body transformation, S_{0i} denotes an estimate of the propagation of the segment to compensate for the phase difference between the segments. The registration of the point clouds based on Eq. (1) leads to an overlap mismatch between the point clouds explained by position uncertainties during the measurement. The desired registration of the segments is obtained by a correction of the presumed transformation of each segment (see Fig. 2) given by

$$\begin{aligned}\mathbf{T}_{1i} &= \mathbf{R}_{0i}\,\boldsymbol{k}_i^* + \mathbf{T}_{0i}\\ \mathbf{R}_{1i} &= \mathbf{R}_{0i}\,\Re(\boldsymbol{\theta}_i^*)\\ S_{1i} &= S_{0i} + s_i^*\end{aligned} \tag{2}$$

where $\boldsymbol{k}_i^* \in \mathbb{R}^3$ denotes the translational misalignment and $\boldsymbol{\theta}_i^* \in \mathbb{R}^3$ the rotational misalignment ($\Re(\boldsymbol{\theta}_i^*) \in \mathbb{R}^{3\times3}$) of the sensor. $s_i^* \in \mathbb{R}$ denotes the correction of the presumed propagation of the segment. The registering parameters of all segments are collected in $\boldsymbol{A}^{*T} = (..\boldsymbol{a}_i^{*T}..) \in \mathbb{R}^{7\,U}$ with $\boldsymbol{a}_i^{*T} = (\boldsymbol{k}_i^{*T}, \boldsymbol{\theta}_i^{*T}, s_i^*) \in \mathbb{R}^7$. Replacing $\mathbf{T}_{0i}$ with $\mathbf{T}_{1i}$, $\mathbf{R}_{0i}$ with $\mathbf{R}_{1i}$ and S_{0i} with S_{1i} in Eq. (1) results in the desired registration of the segments. Let $d_{ik}(x, y, \boldsymbol{A})$ be the overlap mismatch between segment i and segment k at position (x, y) after an arbitrary correction denoted by $\boldsymbol{A}$. For the desired correction, i.e. $\boldsymbol{A}^*$, the overlap mismatch equals the difference between the measurement errors, i.e.

$$0 = d_{ik}(x, y, \boldsymbol{A}^*) - (e_k(x, y) - e_i(x, y)), \tag{3}$$

where $e_k(x, y)$ and $e_i(x, y)$ denote the measurement errors at position (x,y) of segment k and i, respectively. For details regarding the dependence of the overlap mismatch on $\boldsymbol{A}^*$, it is referenced to [15]. Collecting all the considered local overlap mismatches of all overlapping segment pairs in $\boldsymbol{D} = (..d_{ik}(x_n, y_n)..)^T \in \mathbb{R}^N$ with N being the total number of considered overlap mismatches, Eq. (3) turns into the vector equation

$$\mathbf{0} = \boldsymbol{D}(\boldsymbol{A}^*) - \boldsymbol{\Delta e}, \tag{4}$$

where $\boldsymbol{\Delta e}$ contains the corresponding differences between the measurement errors. Linearization of $\boldsymbol{D}$ around $\boldsymbol{A} = \mathbf{0}$ leads to

$$\boldsymbol{D}(\boldsymbol{A}) = \boldsymbol{D}_0 + \boldsymbol{Q}\boldsymbol{A}, \tag{5}$$

with $\boldsymbol{Q} \in \mathbb{R}^{N \times 7\,U}$. $\boldsymbol{D}_0$ denotes the overlap mismatch of the initial configuration of the segments in FG. In Appendix A. a detailed derivation of $\boldsymbol{Q}$ is presented. For more details on the derivation see [14,15]. If Eq. (24) is a good approximation for $\|\boldsymbol{A}\| \geq \|\boldsymbol{A}^*\|$, Eq. (4) can be written as

$$\boldsymbol{B} = -\boldsymbol{D}_0 = \boldsymbol{Q}\boldsymbol{A}^* - \boldsymbol{\Delta e}, \tag{6}$$

and the linear estimator

$$(\boldsymbol{Q}^T\boldsymbol{Q})^{-1}\boldsymbol{Q}^T\boldsymbol{B} = \hat{\boldsymbol{A}} \tag{7}$$

can be used to estimate $\boldsymbol{A}^*$. For the mean of the errors $E[\boldsymbol{\Delta e}] = 0$ and the covariance matrix of the errors $\boldsymbol{C}_{\boldsymbol{\Delta e}} = \sigma^2_{\Delta e}\boldsymbol{I}$, with $\boldsymbol{I}$ being the identity matrix and $\sigma_{\Delta e}$ being a scalar value, Eq. (7) corresponds to the best linear unbiased estimator proved by the Gauss-Markov theorem [22]. Using a linear estimator, parallel registration can be carried out with low computational costs [14]. A priori information concerning the auto-correlation matrix of $\boldsymbol{A}^*$, i.e. $\boldsymbol{\Lambda} = E[\boldsymbol{A}^*\boldsymbol{A}^{*T}]$, can be incorporated by the estimator [23]

$$(\boldsymbol{Q}^T\boldsymbol{C}^{-1}_{\boldsymbol{\Delta e}}\boldsymbol{Q} + \boldsymbol{\Lambda}^{-1})^{-1}\boldsymbol{Q}^T\boldsymbol{C}^{-1}_{\boldsymbol{\Delta e}}\boldsymbol{B} = \hat{\boldsymbol{A}}. \tag{8}$$

If $\boldsymbol{A}^*$ and $\boldsymbol{\Delta e}$ are uncorrelated and $E[\boldsymbol{\Delta e}] = 0$, Eq. (8) corresponds to the best linear estimator and provides a better estimation than Eq. (7).

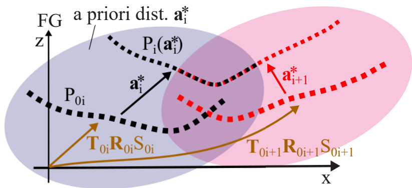

Fig. 2. The segments show an overlap mismatch if they are positioned in FG at the nominal measurement positions, described by $(..\mathbf{T}_{0i}, \mathbf{R}_{0i}, S_{0i}..)$. The estimation of the registering parameters $\boldsymbol{a}_i^* \in \boldsymbol{A}^*$ is improved using a priori probability distributions for the parameters.

This study focuses on the widely used assumption that $\boldsymbol{\Lambda}$ corresponds to a diagonal matrix and $\boldsymbol{C}_{\boldsymbol{\Delta e}} = \sigma^2_{\Delta e}\boldsymbol{I}$, simplifying Eq. (8) to

$$(\boldsymbol{Q}^T\boldsymbol{Q} + w\,\sigma^2_{\Delta e}\boldsymbol{\Lambda}^{-1})^{-1}\boldsymbol{Q}^T\boldsymbol{B} = \hat{\boldsymbol{A}}, \tag{9}$$

with $w = 1$. w is an additional weighting factor of the a priori information to maintain the estimation quality in case of measurement errors with $E[\boldsymbol{\Delta e}]$ deviating from 0. In case of large $\boldsymbol{A}^*$, Eq. (6) might not be true and Eq. (9) does not provide the desired estimation. In such cases, the desired estimation of the registration data can be obtained in several iterations, where in each iteration the estimator is applied [15].

Based on this approach an a priori iterative fast parallel registration (AIFPR) algorithm is

Research Article | Vol. 30, No. 23 / 7 Nov 2022 / *Optics Express* 41477
Optics EXPRESS

proposed. The algorithm is initialised with the presumed transformations for the registration of the segments. The transformations are collected in $Tr_0 = \{.., \mathbf{T}_{0i}, \mathbf{R}_{0i}, S_{0i}, ..\}$. In the first step, the negative initial overlap mismatch $\boldsymbol{B}$ and the matrix $\boldsymbol{Q}$ of Eq. (24) are computed for the configuration of the segments in FG based on Tr_0. Then the estimator of Eq. (9) is applied leading to $\hat{\boldsymbol{A}}$ and the presumed transformation Tr_0 is corrected to $Tr_1 = \{.., \mathbf{T}_{1i}, \mathbf{R}_{1i}, S_{1i}, ..\}$ using Eq. (2). As mentioned above, the desired estimation might not be obtained ($\hat{\boldsymbol{A}} \neq \boldsymbol{A}^*$) if $\boldsymbol{A}^*$ is of large value. Nevertheless, the corrected transformation Tr_1 provides a better configuration of the segments with a smaller overlap mismatch than the configuration based on Tr_0. The quality of the correction correlates with the quality of the linearisation in Eq. (24) for $\boldsymbol{A} = \hat{\boldsymbol{A}}$. With w in Eq. (9) the quality of the correction can be controlled, as w, in addition to $\boldsymbol{\Lambda}$, can restrict $\hat{\boldsymbol{A}}$ to values for which Eq. (24) provides an acceptable approximation. For a further correction, Tr_1 is considered as the presumed transformation for the registration of the segments and Eq. (9) is applied again to estimate $\boldsymbol{A}_1^*$. To enable the estimation with Eq. (9) an auto-correlation matrix for $\boldsymbol{A}_1^*$, i.e. $\boldsymbol{\Lambda}_1$ has to be determined. For $\boldsymbol{\Lambda}_1$ being diagonal, only the standard deviations of the parameters in $\boldsymbol{A}_1^*$, collected in $\boldsymbol{V}_1 = (..\sigma_{1m}..)^T$, need to be considered as they entirely define the auto-correlation matrix. The proposed updating rule of the standard deviations is

$$\boldsymbol{V}_1 = max(\boldsymbol{V}/\alpha, \boldsymbol{V} - |\hat{\boldsymbol{A}}_g|/\beta), \tag{10}$$

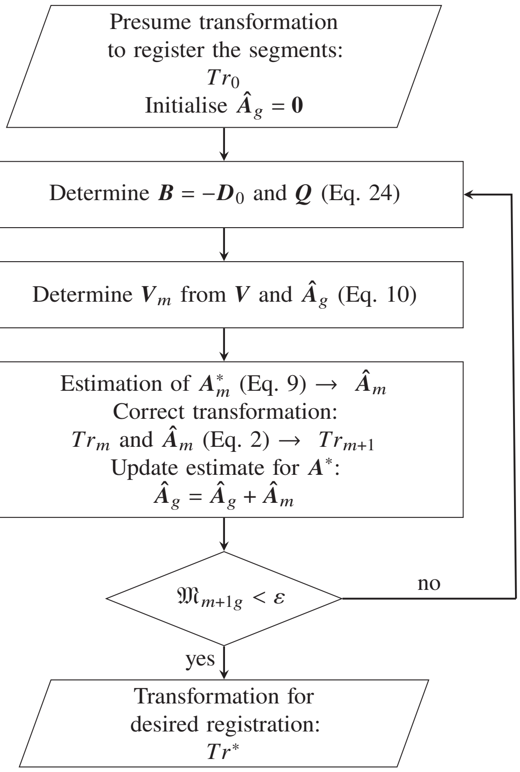

Fig. 3. Flow chart of the AIFPR algorithm.

Published version of the article: Nikolaus Berlakovich, Martin Fuerst, Ernst Csencsics, and Georg Schitter, "Improving the precision of parallel registration by incorporating a priori information," *Optics Express* Vol. 30, Issue 23, pp. 41473-41491, 2022. DOI: 10.1364/OE.469299

where $\boldsymbol{V}$ includes the standard deviations of $\boldsymbol{A}^*$ and α and β are scalar values. $\hat{\boldsymbol{A}}_g$ is the so far estimate for $\boldsymbol{A}^*$ being $\hat{\boldsymbol{A}}$ in this case. With the estimate of $\boldsymbol{A}_1^*$, i.e. $\hat{\boldsymbol{A}}_1$, $\hat{\boldsymbol{A}}_g = \hat{\boldsymbol{A}} + \hat{\boldsymbol{A}}_1$. The second argument in Eq. (10) restricts $\hat{\boldsymbol{A}}_g$ in a certain way to the interval $[-\beta\boldsymbol{V}, \beta\boldsymbol{V}]$ meaning that $\boldsymbol{V}_1$ decreases the closer $\hat{\boldsymbol{A}}_g$ is to $\beta\boldsymbol{V}$. The first argument in Eq. (10) softens this restriction by setting a minimal value for $\boldsymbol{V}_1$. This accelerates the registration and allows registration even in the rare cases, where $\boldsymbol{A}^*$ is outside the interval $[-\beta\boldsymbol{V}, \beta\boldsymbol{V}]$. Estimation of the parameters and correction of the transformation is then repeated until the relative change of the initial overlap mismatch is smaller than a specific threshold (ε) indicating the convergence to the desired transformation Tr^* to register the segments. To enable the comparison of the overlap mismatch to a scalar value, the initial global mismatch metric, defined by $\boldsymbol{D}_0^T\boldsymbol{D}_0/N$ is considered, with N denoting the number of elements in $\boldsymbol{D}_0$. The relative change of the initial global mismatch metric from iteration m to $m+1$ is then given by

$$\Delta\mathfrak{M}_{m+1g} = \frac{|\boldsymbol{D}_{0m+1}^T\boldsymbol{D}_{0m+1} - \boldsymbol{D}_{0m}^T\boldsymbol{D}_{0m}|}{\boldsymbol{D}_{0m}^T\boldsymbol{D}_{0m}}. \tag{11}$$

The steps of the AIFPR algorithm are illustrated in the flowchart in Fig. 3.

3. Algorithm analysis

The performance of the AIFPR algorithm is analysed and compared with an iterative fast parallel registration (IFPR) algorithm [15] and with the established iterative closest point (ICP) algorithm [24]. Using simulation tools, the dependence of the performance of the algorithms on sensor misalignment, measurement noise and the weighting factor of the a priori information (see Eq. (9)) is evaluated. In addition, the algorithms are applied to reconstruct a measured divergent wavefront.

3.1. Simulation setting

Software tools are developed to simulate the measurement of a wavefront with a SHS. The software is based on MATLAB (The MathWorks Inc., Natick, MA, USA) and OpticStudio (Zemax LLC, Kirkland, WA, USA) where the latter one is used for raytracing simulation. In the simulative analysis of the algorithms two use cases are considered including the registration of a freeform wavefront and a divergent wavefront.

The *freeform wavefront* (diameter 50 mm) contains large dynamics with a peak-to-valley (PV) of 587 μm and is simulatively measured in 25 overlapping sub-measurements arranged in the x,y-plane as illustrated in Fig. 4(a). Each sub-measurement corresponds to the measurement with a squared sensor aperture of 13 mm side length. The sub-measurements overlap in an area which is 20 % of the area of the sensor aperture.

The dynamics of the *divergent wavefront* (divergence 140°) have a PV of 61 μm with respect to the nominal sphere of the wavefront with a diameter of 30 mm. The wavefront is simulatively measured in 43 sub-measurements with a circular sensor aperture (diameter 7 mm) arranged on the nominal sphere of the wavefront depicted in Fig. 4(b). The overlap area between some sub-measurements is larger than 20 % of the sensor aperture to allow for a complete covering of the wavefront.

From the sub-measurements the segments of the wavefront are then reconstructed using a spline-based zonal reconstruction algorithm [25]. The reconstruction of the segments is followed by the registration of the segments using the registration algorithms reconstructing the entire wavefront. The local overlap mismatches at all points belonging to the overlap area of the point cloud are used for registration and are considered in $\boldsymbol{D}$ (see Eq. (24)), resulting in 930 and 315 average number of points per overlap used for registration of the freeform and the divergent wavefront respectively. In the AIFPR and the IFPR algorithm the point clouds of the segments are interpolated using cubic interpolation and the normal vectors are interpolated using linear

Published version of the article: Nikolaus Berlakovich, Martin Fuerst, Ernst Csencsics, and Georg Schitter, "Improving the precision of parallel registration by incorporating a priori information," *Optics Express* Vol. 30, Issue 23, pp. 41473-41491, 2022. DOI: 10.1364/OE.469299

Optics EXPRESS

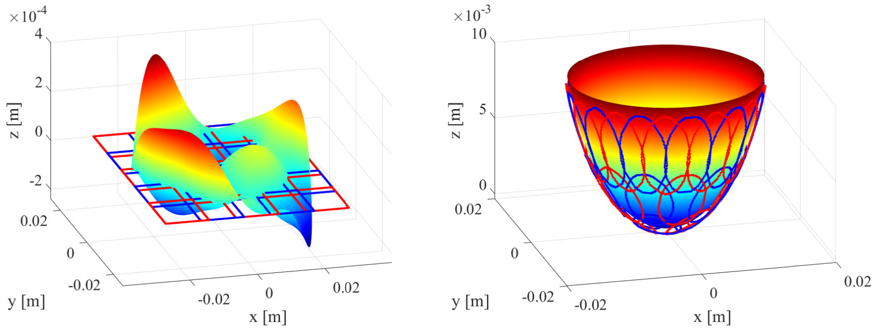

(a) (b)

Fig. 4. The freeform wavefront (PV=587 μm) measured at 25 sensor positions (a) and the divergent wavefront (divergence=140°, PV=61 μm with respect to the nominal sphere with diameter 30 mm) measured at 43 sensor positions (b). The measurement of the wavefronts is simulated.

interpolation [14] to enable subpixel registration. The stopping conditions of the AIFPR and IFPR algorithm (see Fig. 3) use the same threshold of $\varepsilon = \frac{1}{3}$ which is a suitable value for fast convergence [15]. For the updating rule of the standard deviations of the registering parameters in each iteration (see Eq. (10)), α is set to a value of 5 and β to a value of 2. These values turned out to be good choices for Gaussian distributed sensor misalignment which is considered in the simulation of the measurements.

While the AIFPR and IFPR algorithm register the segments in parallel, the ICP algorithm registers the segments sequentially, meaning that the segments are consecutively combined in individual registration processes where in each registration process one segment is added to the entire wavefront. The segments are combined in a spiral way starting from the segment in the center of the set of segments [12]. To evaluate the registration performance, the reconstructed wavefront is fitted into the original wavefront. Then the difference between the reconstructed and the original wavefront is determined. A non-zero difference between the wavefronts may result from registration errors, measurement noise and systematic measurement errors. Removing the simulated measurement errors from the difference reveals the registration error over the aperture of the wavefront. In a last step the root-mean-square (RMS) and the PV of the registration error are computed to enable a comparison of different registration results.

3.2. *Reference configuration*

To obtain a realistic simulation, noise as well as sensor misalignment is simulated. The measurement noise is Gaussian distributed with zero mean and a standard deviation $\sigma = 10\,nm$. For each point in the point cloud representing a segment, a measurement noise is drawn from the underlying probability distribution and added to the point. The sensor misalignment during the measurement of segment i is reflected by the registering parameters $\boldsymbol{k}_i^*, \boldsymbol{\theta}_i^* \in \mathbb{R}^3$ (see Eq. (2)) where $\boldsymbol{k}_i^*$ denotes translational misalignment and $\boldsymbol{\theta}_i^*$ rotational misalignment of the sensor. The simulated sensor misalignment is Gaussian distributed with zero mean where the elements of $\boldsymbol{k}_i^*$ have a standard deviation $\sigma = 40\,\mu m$ and those of $\boldsymbol{\theta}_i^*$ a standard deviation $\sigma = 1.2\,mrad$. The standard deviations have realistic values considering a multi-axis positioning system [17]. The weighting factor in the estimator of the AIFPR algorithm (see Eq. (9)) is set to 100.

Published version of the article: Nikolaus Berlakovich, Martin Fuerst, Ernst Csencsics, and Georg Schitter, "Improving the precision of parallel registration by incorporating a priori information," *Optics Express* Vol. 30, Issue 23, pp. 41473-41491, 2022. DOI: 10.1364/OE.469299

The *freeform wavefront* is reconstructed by the algorithms with a registration error illustrated in Fig. 5. The RMS registration error of the AIFPR algorithm is 11 *nm* which is a factor of 3 smaller than the RMS registration error of the IFPR algorithm.

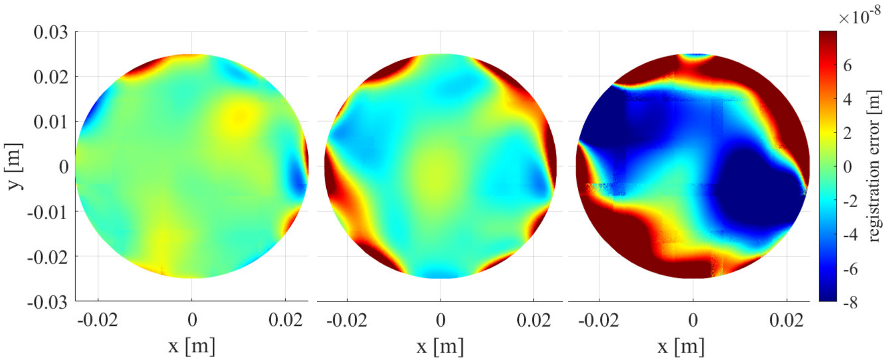

(a) AIFPR
RMS = 11 *nm*, PV = 180 *nm*

(b) IFPR
RMS = 30 *nm*, PV = 380 *nm*

(c) ICP
RMS = 110 *nm*, PV = 955 *nm*

Fig. 5. Registration error of the AIFPR (a), IFPR (b) and ICP (c) algorithm for the freeform wavefront with respect to the exact wavefront.

For the *divergent wavefront* the related registration error of the algorithms is illustrated in Fig. 6. With an RMS registration error of 30 *nm* the AIFPR algorithm attains a registration result a factor of 2 better than the IFPR algorithm.

The results show the improvement that can be attained by incorporating the standard deviation of the sensor misalignment. Using the a priori information, the segments are prevented from too large translation and rotation during the registration. Reasons for too large registering parameters are translational or rotational symmetries of the segments as well as approximation errors due to the linearization of the overlap mismatch in Eq. (24). The dependence of the registration error on the shape of the wavefront, the number of registered segments as well as the number of points per overlap used for registration [14,15] might be the reason for the slightly better registration results with respect to the freeform wavefront as compared to the divergent wavefront. The reduced registration quality using the ICP algorithm as compared to the other algorithms is explained by the sequential approach of registering the segments, which leads to an increased accumulation of registration errors. In addition, the ICP algorithm does not consider propagation of the segments, resulting in large registration errors for the divergent wavefront.

The AIFPR and the IFPR algorithm show both fast convergence to the minimum of the global mismatch metric, which is for both wavefronts reached in 3 iterations as illustrated in Fig. 7. The global mismatch metric is given by $\boldsymbol{D}_{0m}^T \boldsymbol{D}_{0m}/N$ for iteration m (see Eq. (11)). The algorithms run on a personal computer with a processor frequency of 2.6 *GHz*. The AIFPR and IFPR algorithm have comparable computation times around 300 *ms* for both wavefronts. The ICP algorithm needs around 2 *s* to register the wavefronts.

In the following sections the values of the simulated sensor misalignment and measurement noise and the weighting factor of the a priori information are equivalent to those of the reference configuration if no other values are explicitly mentioned.

3.3. Influence weighting factor of a priori information

In each iteration of the AIFPR algorithm, linearization of the local overlap mismatches is carried out (see Eq. (24)) followed by the estimation of the registering parameters (see Eq. (9)). Large

Published version of the article: Nikolaus Berlakovich, Martin Fuerst, Ernst Csencsics, and Georg Schitter, "Improving the precision of parallel registration by incorporating a priori information," *Optics Express* Vol. 30, Issue 23, pp. 41473-41491, 2022. DOI: 10.1364/OE.469299

Optics EXPRESS

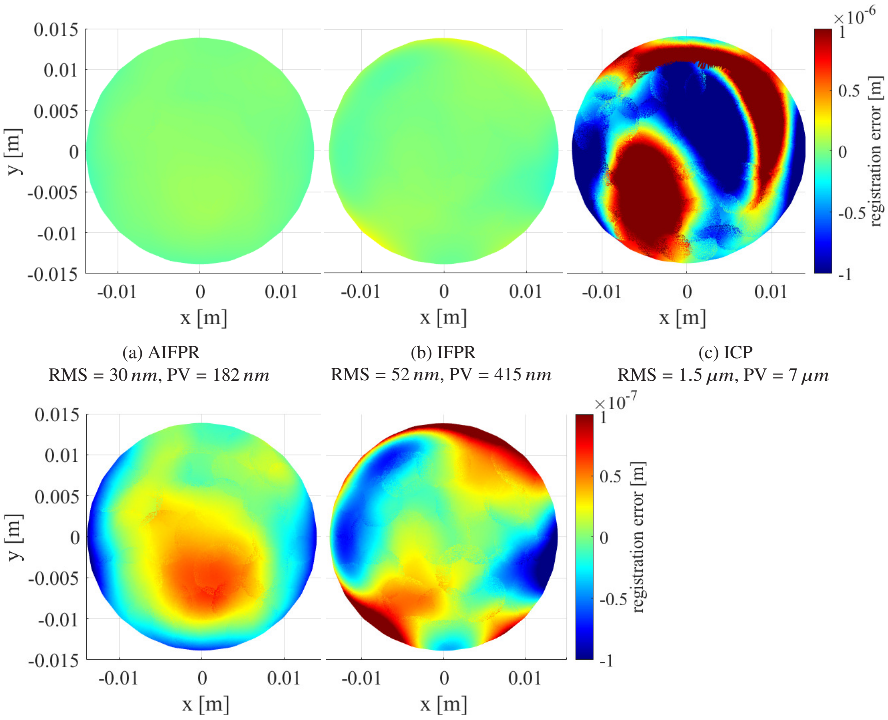

(a) AIFPR
RMS = 30 nm, PV = 182 nm

(b) IFPR
RMS = 52 nm, PV = 415 nm

(c) ICP
RMS = 1.5 μm, PV = 7 μm

(d) AIFPR
RMS = 30 nm, PV = 182 nm

(e) IFPR
RMS = 52 nm, PV = 415 nm

Fig. 6. Registration error of the AIFPR (a,d), IFPR (b,e) and ICP (c) algorithm for the divergent wavefront with respect to the exact wavefront. Figure (d) and (e) show the same results as (a) and (b) but at a different scale for a better visualization of details of the registration error.

registering parameters are estimated with large errors, as Eq. (24) is not valid for large values of $\boldsymbol{A}$. In the estimator $w \in \mathbb{R}$ denotes a weighting factor of the a priori information where $w > 1$ can be used to restrict the estimation of the registering parameters ($\hat{\boldsymbol{A}}$) to values for which Eq. (24) provides an acceptable approximation resulting in reduced estimation errors. A mean of the difference between the measurement errors ($E[\boldsymbol{\Delta e}]$) deviating from 0 results in a decrease of the quality of the estimator especially for a large number of points per overlap used for registration. In such a case, the quality of the estimator can be maintained using $w > 1$. In Fig. 8 the RMS registration error of the AIFPR algorithm is illustrated in dependence of the weighting factor of the a priori information for the freeform and the divergent wavefront. Results show that a weighting factor in the range between 10 and 100 improves the registration by a factor of 3. For excessive weighting factors of 10000 the registration errors again significantly increase, as in this case the estimation is restricted to too small values for the respective registering parameters.

3.4. Influence of sensor misalignment

Misalignment of the sensor refers to a deviation from the sensor's nominal position and alignment and is caused by uncertainties in the positioning system [17]. Translational and rotational misalignment during the measurement of segment i is reflected by the corresponding registering

Published version of the article: Nikolaus Berlakovich, Martin Fuerst, Ernst Csencsics, and Georg Schitter, "Improving the precision of parallel registration by incorporating a priori information," *Optics Express* Vol. 30, Issue 23, pp. 41473-41491, 2022. DOI: 10.1364/OE.469299

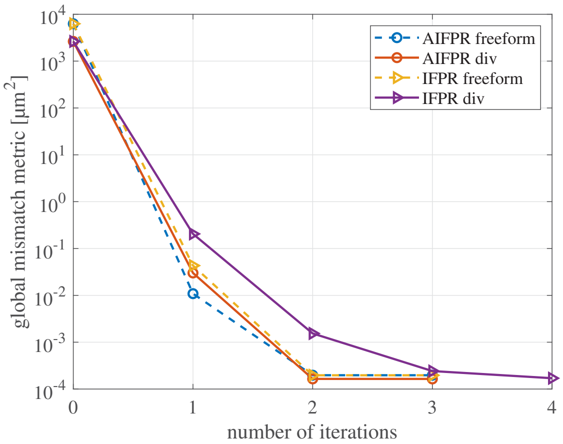

Fig. 7. Minimization of the global mismatch metric (see Eq. (11)) in dependence of the number of iterations of the AIFPR and the IFPR algorithm in case of the freeform and divergent wavefront. The measurement conditions are with respect to the reference configuration.

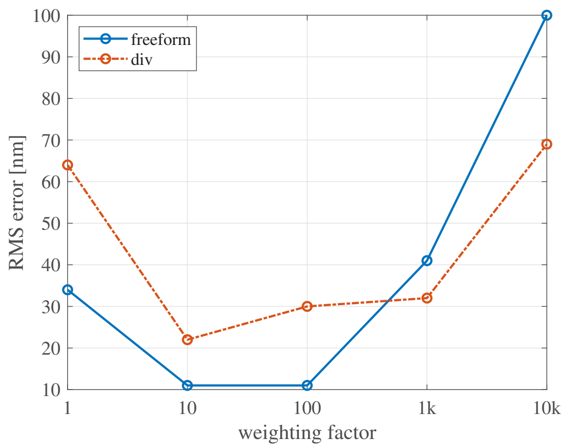

Fig. 8. RMS registration error of the AIFPR algorithm in dependence of the weighting factor of a priori information for the freeform (blue) and the divergent wavefront (red) with respect to the simulation settings of the reference configuration.

Published version of the article: Nikolaus Berlakovich, Martin Fuerst, Ernst Csencsics, and Georg Schitter, "Improving the precision of parallel registration by incorporating a priori information," *Optics Express* Vol. 30, Issue 23, pp. 41473-41491, 2022. DOI: 10.1364/OE.469299

parameters $\boldsymbol{k}_i^* \in \mathbb{R}^3$ and $\boldsymbol{\theta}_i^* \in \mathbb{R}^3$ respectively (see Eq. (2)). The RMS registration error of the algorithms in dependence of the standard deviation of the translational misalignment is shown in Fig. 9(a) and Fig. 9(b) for the freeform and the divergent wavefront, respectively. The dependence of the RMS registration error on the translational misalignment is determined in presence of rotational misalignment one time with $\sigma = 1.2\,mrad$ and one time with $\sigma = 2.4\,mrad$.

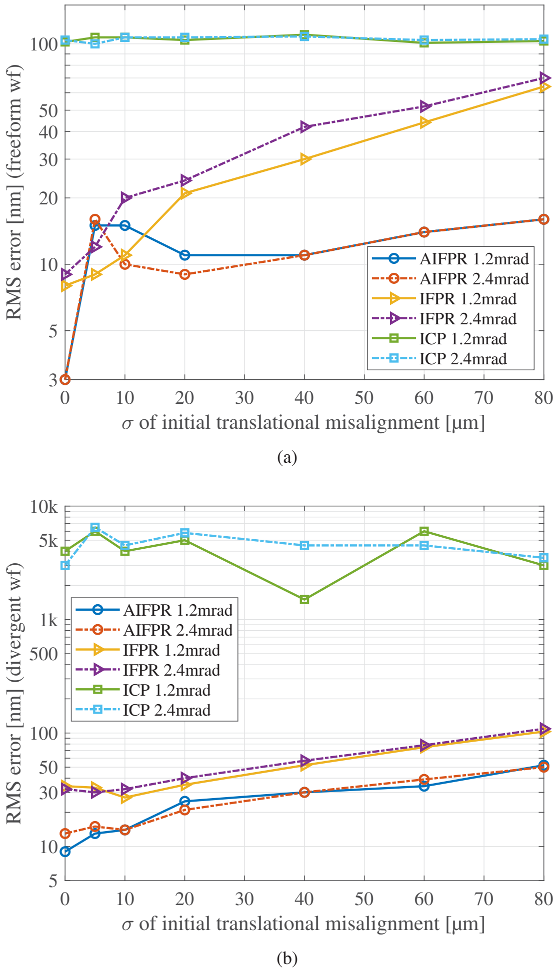

Fig. 9. RMS registration error in dependence of σ of initial translational misalignment for the AIFPR, IFPR and the ICP algorithm regarding the freeform wavefront (a) and the divergent wavefront (b). Curves are shown for two different standard deviations of initial rotational misalignment, i.e. 1.2 and 2.4 *mrad*.

For large misalignment with $\sigma = 80\,\mu m$ the *freeform wavefront* is registered by the AIFPR algorithm with high quality where an RMS registration error of 15 *nm* is attained. For the same misalignment the IFPR algorithm attains a 4 times larger RMS registration error.

Published version of the article: Nikolaus Berlakovich, Martin Fuerst, Ernst Csencsics, and Georg Schitter, "Improving the precision of parallel registration by incorporating a priori information," *Optics Express* Vol. 30, Issue 23, pp. 41473-41491, 2022. DOI: 10.1364/OE.469299

The *divergent wavefront* is registered by the AIFPR algorithm with an RMS registration error of 50 *nm* in case of translational misalignment with $\sigma = 80\,\mu m$. Under the same misalignment conditions the IFPR algorithm attains an RMS registration error of 100 *nm*.

The results show the higher robustness of the AIFPR algorithm to sensor misalignment as compared to the other algorithms. As can be expected, the results of both algorithms deteriorate with an increase of the misalignment where the extent of deterioration is less using the AIFPR algorithm. Results show that an increase of rotational misalignment hardly increases the registration error which is due to the flat shape of the wavefront segments leading to an overlap mismatch that is more sensitive to rotational misalignment than to translational misalignment. For the freeform wavefront the ICP algorithm shows high robustness to misalignment, as the results are hardly affected by an increase of the mislaignment. Nevertheless, the results of the ICP algorithm are of less quality as compared to the other algorithms, explained by the increased accumulation of registration errors for sequential registration.

3.5. Influence of noise and systematic error

Measurement noise caused by, e.g., background light, readout and dark currents [26] is simulated by adding a Gaussian distributed error with a zero mean value to each point in the point cloud of a segment. In addition to noise, the residual systematic error after a calibration of the SHS [27] is simulated in this section. For this purpose an error distribution with a PV equal to 5 *nm* is added to each point cloud. In Fig. 10 the RMS registration error of the algorithms in dependence of the standard deviation of measurement noise up to 20 *nm* is illustrated for both wavefronts. As expected, the RMS registration error of the algorithms increases with a larger standard deviation of noise. The AIFPR algorithm attains the best results with a RMS error below 20 *nm* for the freefrom and 30 *nm* for the divergent wavefront. While the performance of the IFPR algorithm decreases by a factor of 3 when noise is increased to $\sigma = 20\,nm$, its performance is less affected by noise for the divergent wavefront. This implies the dependence of the robustness of the algorithms on the shape of the wavefront. For the divergent wavefront the results of the ICP algorithm cannot be evaluated for noise with $\sigma > 10\,nm$ due to huge gaps in the reconstructed wavefront.

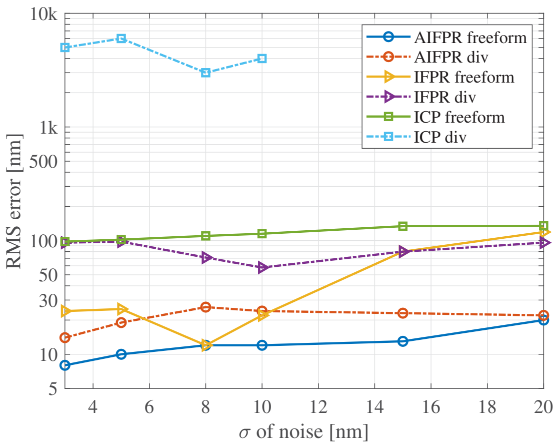

Fig. 10. RMS registration error in dependence of σ of the measurement noise for the AIFPR, IFPR and the ICP algorithm considering the freeform and the divergent wavefront. In addition to noise, a systematic measurement error is simulated with a $PV = 5\,nm$.

Published version of the article: Nikolaus Berlakovich, Martin Fuerst, Ernst Csencsics, and Georg Schitter, "Improving the precision of parallel registration by incorporating a priori information," *Optics Express* Vol. 30, Issue 23, pp. 41473-41491, 2022. DOI: 10.1364/OE.469299

4. Experimental setup and results

The measurement system is realized with a commercial SHS (HR-2, Optocraft, Erlangen, Germany) mounted on a multi-axis positioning system consisting of three linear stages (VT-80, PI Physik Instrumente, Braunschweig, Germany) and two rotational stages (RM-3, Newmark Systems Inc., California) as illustrated in Fig. 11. An arbitrary configuration of position and alignment of the sensor can be realized with the multi-axis positioning system to allow for scanning of complex shaped wavefronts. For the positioning uncertainty of the sensor a standard deviation of $\sigma = 20\,\mu m$ for the translational and $\sigma = 1\,mrad$ for the rotational misalignment is expected. A microscope objective (NA=0.45) is illuminated with a collimated beam to generate a wavefront with a divergence of approximately 54°. A measurement with the SHS is carried out at 43 locations of the wavefront resulting in 43 segments that are registered by the algorithms.

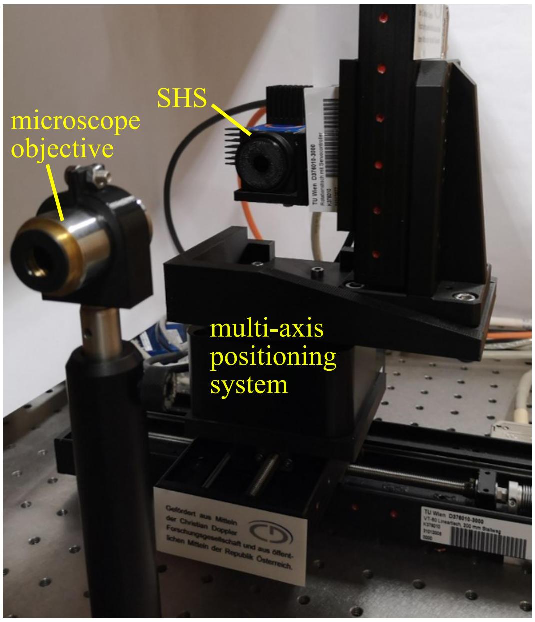

Fig. 11. Setup for the measurement of the wavefront of a microscope objective with an NA=0.45. The sensor is positioned via a multi-axis positioning system.

The reconstructed wavefront of the AIFPR and IFPR algorithm is depicted in Fig. 12(a) and Fig. 12(b) respectively. The nominal wavefront, i.e. a sphere, is fitted into the reconstructed wavefront and the difference between nominal and reconstructed wavefront is shown in Fig. 12(c) and Fig. 12(d) for the results of the AIFPR and IFPR algorithm. The illustrated difference (e_{tot}) has an RMS value of 71 nm and 81 nm for the AIFPR and the IFPR algorithm respectively and corresponds to the sum of wavefont aberration and registration error, i.e. $e_{tot} = e_{ab} + e_{reg}$. Assuming no correlation between e_{ab} and e_{reg} and a zero mean value for e_{reg} or e_{ab}, the RMS value of e_{tot} can be written as

$$RMS_{tot} = \sqrt{RMS_{ab}^2 + RMS_{reg}^2}, \tag{12}$$

where RMS_{ab} and RMS_{reg} are the RMS values of e_{ab} and e_{reg}. Considering the simulative analysis, a value for RMS_{reg} of around 30 nm is expected from the AIFPR algorithm, which results in

Published version of the article: Nikolaus Berlakovich, Martin Fuerst, Ernst Csencsics, and Georg Schitter, “Improving the precision of parallel registration by incorporating a priori information,” *Optics Express* Vol. 30, Issue 23, pp. 41473-41491, 2022. DOI: 10.1364/OE.469299

RMS_{ab} = 64 *nm* using Eq. (12). With this RMS value for the wavefront aberration the RMS registration error of the IFPR algorithm is around RMS_{reg} = 50 *nm*, which is comparable to the results of the simulation (see Fig. 6). The results of the ICP algorithm are not explicitly illustrated, as they contain huge registration errors leading to an insufficient reconstruction of the wavefront. The measurement of the wavefront is repeated and for each measurement the wavefront is reconstructed using the AIFPR and IFPR algorithm. Deviations between the results are caused due to statistical variations of the measurement errors and the sensor misalignment. For 10 measurements of the wavefront the values for RMS_{tot} have a mean value of 71 *nm* and a standard deviation of 1.6 *nm* for the AIFPR algorithm and a mean value of 84 *nm* and a standard deviation of 12 *nm* for the IFPR algorithm. The results proof the higher robustness of the AIFPR algorithm to measurement errors and sensor misalignment as compared to the IFPR algorithm.

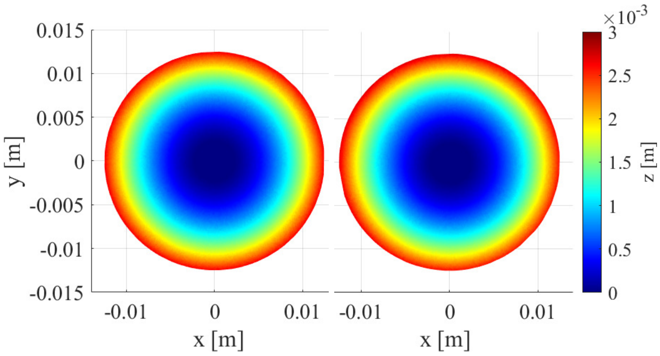

(a) AIFPR
reconstructed wavefront

(b) IFPR
reconstructed wavefront

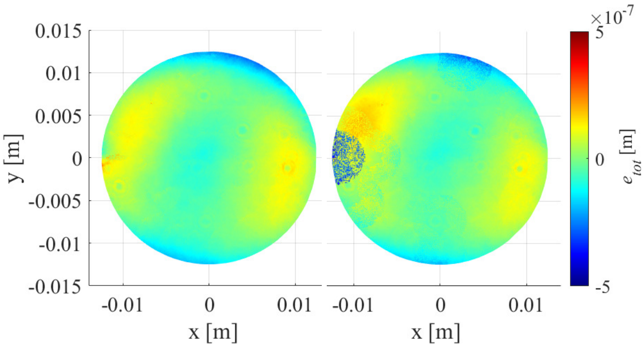

(c) AIFPR
RMS = 71 *nm*, PV = 545 *nm*

(d) IFPR
RMS = 81 *nm*, PV = 655 *nm*

Fig. 12. Wavefront of a microscope objective (NA=0.45) registered by the AIFPR (a) and IFPR (b) algorithm and the corresponding difference (e_{tot}) from a spherical wavefront (AIFPR (c), IFPR (d)). The wavefront is measured in 43 segments.

In summary, the improved registration performance of the proposed a priori iterative fast parallel registration algorithm as compared to an IFPR algorithm and the ICP algorithm is successfully demonstrated. The algorithm attains small registration errors, which can be a factor of 3 smaller than those of the IFPR algorithm and a factor of 50 smaller than those of the ICP algorithm if highly divergent wavefronts are considered. The algorithm shows fast convergence to the registering parameters and needs computation times of a few hundred milliseconds on a personal computer.

5. Conclusions

In this paper, an algorithm is proposed for the high-quality registration of a set of optical wavefronts. The algorithm is able to incorporate a priori information about the positioning uncertainty of the sensor during the measurement of the wavefronts resulting in an improved registration performance. Parallel registration of the wavefronts is enabled by the algorithm allowing for a reduced accumulation of registration errors. The algorithm's high degree of flexibility with respect to the shape of the wavefront makes it suitable for the reconstruction of freeform as well as highly divergent wavefronts. The mathematics of the algorithm are discussed and an analysis of the algorithm is presented, where it is compared to an IFPR algorithm [15] and the ICP algorithm. Using simulations, the performance of the algorithm is evaluated with respect to sensor misalignment and measurement errors and it is shown that the algorithm attains RMS registration errors down to 10 *nm*. Even for large sensor misalignment with a standard deviation of 80 *µm* and 2.4 *mrad* the algorithm reconstructs a freeform and a divergent wavefront with an RMS registration error of a few tens of nanometers and attains results a factor of 2 to 3 better than the other algorithms. Only 3 iterations are required to obtain the results for both wavefronts leading to a total computation time of around 300 *ms* on a personal computer. In addition to the simulative evaluation, the algorithm is applied to a real divergent wavefront generated by a microscope objective with an NA=0.45. Results show that the algorithm reconstructs the wavefront with a higher quality as compared to the IFPR and the ICP algorithm. The low computation times and the high registration accuracy despite large sensor misalignment and measurement errors make the algorithm suitable for time critical measurement tasks of high-end optical systems.

A. Linearization of the overlap mismatch

Two propositions are introduced in the following, which are used to derive the formulas for the linearization of the overlap mismatch.

Proposition 1 *An arbitrary translation of a plane given by the vector* $\boldsymbol{t}$ *is equivalent to a translation of the plane given by* $\boldsymbol{n} \cdot \rho$*, where* $\boldsymbol{n}$ *is the unit normal vector of the plane and* $\rho \in \mathbb{R}$ *is a scalar value given by*

$$\boldsymbol{n}^T \boldsymbol{t} = \rho. \tag{13}$$

With Fig. 13 and the well known definition of the dot product ($\boldsymbol{n}^T \boldsymbol{t} = |\boldsymbol{n}|\,|\boldsymbol{t}|\,cos(\gamma)$) Proposition 1 is obvious.

Proposition 2 *A translation of a plane given by* $\boldsymbol{n} \cdot \rho$*, where* $\boldsymbol{n}$ *is the unit normal vector of the plane and* $\rho \in \mathbb{R}$ *is a scalar value, is in a coordinate system L equivalent to a translation along the z-axis given by*

$$\frac{\rho}{n_z^{\{L\}}} = \Delta z, \tag{14}$$

where $n_z^{\{L\}}$ *is the z-component of* $\boldsymbol{n}$ *represented in L.*

Proof. *From Fig. 13 and the fact that* $\boldsymbol{n}$ *is a unit vector the following equation can derived.*

$$sin(\alpha) = \frac{\rho}{\Delta z} = n_z^{\{L\}} \rightarrow \frac{\rho}{n_z^{\{L\}}} = \Delta z \quad \blacksquare$$

The local overlap mismatch between two wavefront segments (index 1 and 2) at a sampling point ($\boldsymbol{q}_{21n}$) is given by

$$d_{12}(\boldsymbol{q}_{21n}, \mathbf{a}_1, \mathbf{a}_2) = W_2^{\{1\}}(\boldsymbol{q}_{21n}, \mathbf{a}_2) - W_1^{\{1\}}(\boldsymbol{q}_{21n}, \mathbf{a}_1), \tag{15}$$

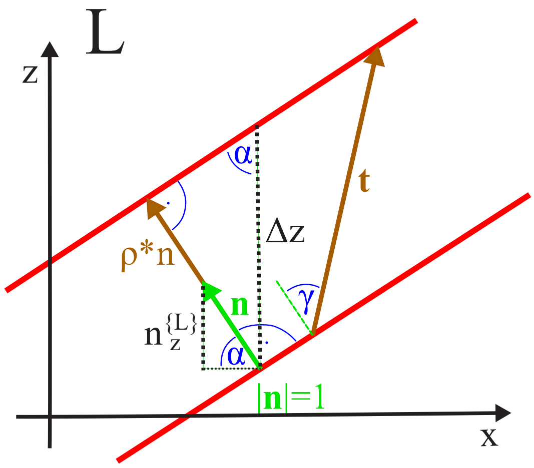

Fig. 13. Translation of a plane by $\boldsymbol{t}$ or $\boldsymbol{n} \cdot \rho$, where $\boldsymbol{n}$ is the unit normal vector of the plane and $\rho \in \mathbb{R}$ is a scalar value.

where $W_1^{\{1\}}(\cdot, \mathbf{a}_1) = W_1^{\{1\}}(\mathbf{a}_1)$ and $W_2^{\{1\}}(\cdot, \mathbf{a}_2) = W_2^{\{1\}}(\mathbf{a}_2)$ are functions describing segment 1 and 2, respectively, in the local coordinate system of segment 1 (see Fig. 14), i.e. FS1, indicated by the upper index in curly brackets. $\boldsymbol{q}_{21n} \in \mathbb{R}^2$ denotes a sampling point in the x-y plane of FS1 belonging to the overlapping region of the segments. The transformation of segment 1 and 2 is defined by $\mathbf{a}_1$ and $\mathbf{a}_2$, respectively, with $\mathbf{a}_i^T = (\mathbf{k}_i^T, \boldsymbol{\theta}_i^T, s_i) \in \mathbb{R}^7$. Let $\boldsymbol{\chi}_n$ be a point of $W_2(\mathbf{a}_2 = \mathbf{0})$, i.e. segment 2 not transformed, with $\boldsymbol{\eta}_n$ denoting the unit normal vector of segment 2 at $\boldsymbol{\chi}_n$. The transformation of segment 2 by $\mathbf{a}_2$ is in the local coordinate system of segment 2 defined by

$$\boldsymbol{\chi}_n^{\{2\}}(\mathbf{a}_2) = \Re(\boldsymbol{\theta}_2)\,(\boldsymbol{\chi}_n^{\{2\}} + s_2\,\boldsymbol{\eta}_n^{\{2\}}) + \mathbf{k}_2, \tag{16}$$

where $\boldsymbol{k}_2 \in \mathbb{R}^3$ denotes a translation, $\boldsymbol{\theta}_2 \in \mathbb{R}^3$ denotes a rotation about the three spatial dimensions ($\Re(\boldsymbol{\theta}_2) \in \mathbb{R}^{3\times 3}$) and $s_2 \in \mathbb{R}$ denotes a wavefront propagation. With the assumption that the considered transformation parameters are small, linearization of Eq. (16) leads to

$$\boldsymbol{\chi}_n^{\{2\}}(\mathbf{a}_2) = \boldsymbol{\chi}_n^{\{2\}} + \mathbf{k}_2 + \sum_{v=1}^{3} \Re'_v\,\boldsymbol{\chi}_n^{\{2\}}\,\theta_{2v} + s_2\,\boldsymbol{\eta}_n^{\{2\}}, \tag{17}$$

which is obtained after a Taylor expansion of Eq. (16) and neglecting second order terms with respect to the parameters. $\Re'_v = \frac{d\Re(\boldsymbol{\theta})}{d\theta_v}|_{\boldsymbol{\theta}=\mathbf{0}}$ with θ_v being a component of $\boldsymbol{\theta}$.

In the vicinity of $\boldsymbol{\chi}_n$ segment 2 can be approximated by a plane including $\boldsymbol{\chi}_n$ with a surface normal vector equal to $\boldsymbol{\eta}_n$, which can be proven with a Taylor expansion of the wavefront about $\boldsymbol{\chi}_n$. Considering Eq. (17) the transformation of segments 2 leads to a translation of the plane by the vector

$$\boldsymbol{t}_n^{\{2\}} = \mathbf{k}_2 + \sum_{v=1}^{3} \Re'_v\,\boldsymbol{\chi}_n^{\{2\}}\,\theta_{2v} + s_2\,\boldsymbol{\eta}_n^{\{2\}}. \tag{18}$$

With Proposition 1, this translation is equivalent to the translation of the plane by $\boldsymbol{\eta}_n^{\{2\}} \cdot \rho$ with

$$\rho = \boldsymbol{\eta}_n^{\{2\}\,T}\,\boldsymbol{t}_n^{\{2\}} = \boldsymbol{\eta}_n^{\{2\}\,T}\,\mathbf{k}_2 + \sum_{v=1}^{3} \boldsymbol{\eta}_n^{\{2\}\,T}\,\Re'_v\,\boldsymbol{\chi}_n^{\{2\}}\,\theta_{2v} + s_2. \tag{19}$$

Published version of the article: Nikolaus Berlakovich, Martin Fuerst, Ernst Csencsics, and Georg Schitter, "Improving the precision of parallel registration by incorporating a priori information," *Optics Express* Vol. 30, Issue 23, pp. 41473-41491, 2022. DOI: 10.1364/OE.469299

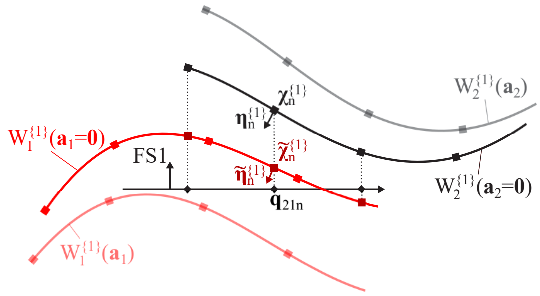

Fig. 14. Segment 1 ($W_1(\mathbf{a}_1)$) and segment 2 ($W_2(\mathbf{a}_2)$) in the local coordinate system of segment 1 (FS1) [14].

The last term includes only s_2, as $\boldsymbol{\eta}_n^{\{2\}\,T}\boldsymbol{\eta}_n^{\{2\}} = 1$. With Proposition 2 the translation of the plane by $\boldsymbol{\eta}_n^{\{2\}} \cdot \rho$ is in the local coordinate system of segment 1 equivalent to a change of the height of the plane by

$$\Delta z = \frac{\rho}{\eta_{nz}^{\{1\}}} = \frac{1}{\eta_{nz}^{\{1\}}}\left[\boldsymbol{\eta}_n^{\{2\}\,T}\mathbf{k}_2 + \sum_{v=1}^{3}\boldsymbol{\eta}_n^{\{2\}\,T}\mathfrak{R}'_v\boldsymbol{\chi}_n^{\{2\}}\,\theta_{2v} + s_2\right], \tag{20}$$

where $\eta_{nz}^{\{1\}}$ is the z-component of $\boldsymbol{\eta}_n^{\{1\}}$. With Eq. (20) the transformed segment 2 in the local coordinate system of segment 1 is given by the function

$$\begin{aligned} W_2^{\{1\}}(\boldsymbol{q}_{21n}, \mathbf{a}_2) &= \chi_{nz}^{\{1\}} + \frac{1}{\eta_{nz}^{\{1\}}}\left[\boldsymbol{\eta}_n^{\{2\}\,T}\mathbf{k}_2 + \sum_{v=1}^{3}\boldsymbol{\eta}_n^{\{2\}\,T}\mathfrak{R}'_v\boldsymbol{\chi}_n^{\{2\}}\,\theta_{2v} + s_2\right] \\ &= \chi_{nz}^{\{1\}} + \boldsymbol{C}_{12n}^T\,\mathbf{a}_2, \end{aligned} \tag{21}$$

if $\boldsymbol{\chi}_n^{\{1\}}$ is the point at $W_2^{\{1\}}(\boldsymbol{q}_{21n}, \mathbf{a}_2 = \mathbf{0})$ (see Fig. 14) where $\chi_{nz}^{\{1\}}$ is the z-component of $\boldsymbol{\chi}_n^{\{1\}}$. $\boldsymbol{C}_{12n} \in \mathbb{R}^7$ contains the coefficients of $\mathbf{a}_2$.

Analogous to the derivation of Eq. (21), an expression for the transformed segment 1 in its local coordinate system can be derived given by

$$\begin{aligned} W_1^{\{1\}}(\boldsymbol{q}_{21n}, \mathbf{a}_1) &= \tilde{\chi}_{nz}^{\{1\}} + \frac{1}{\tilde{\eta}_{nz}^{\{1\}}}\left[\tilde{\boldsymbol{\eta}}_n^{\{1\}\,T}\mathbf{k}_1 + \sum_{v=1}^{3}\tilde{\boldsymbol{\eta}}_n^{\{1\}\,T}\mathfrak{R}'_v\tilde{\boldsymbol{\chi}}_n^{\{1\}}\,\theta_{1v} + s_1\right] \\ &= \tilde{\chi}_{nz}^{\{1\}} + \tilde{\boldsymbol{C}}_{12n}^T\,\mathbf{a}_1, \end{aligned} \tag{22}$$

where $\tilde{\boldsymbol{\chi}}_n^{\{1\}}$ and $\tilde{\boldsymbol{\eta}}_n^{\{1\}}$ are point and normal vector at $W_1^{\{1\}}(\boldsymbol{q}_{21n}, \mathbf{a}_1 = \mathbf{0})$ (see Fig. 14) with $\tilde{\chi}_{nz}^{\{1\}}$ and $\tilde{\eta}_{nz}^{\{1\}}$ as the related z-components. $\tilde{\boldsymbol{C}}_{12n} \in \mathbb{R}^7$ contains the coefficients of $\mathbf{a}_1$.

Inserting Eqs. (21) and (22) into Eq. (15) leads to

$$\begin{aligned} d_{12}(\boldsymbol{q}_{21n}, \mathbf{a}_1, \mathbf{a}_2) &= \chi_{nz}^{\{1\}} + \boldsymbol{C}_{12n}^T\,\mathbf{a}_2 - \tilde{\chi}_{nz}^{\{1\}} - \tilde{\boldsymbol{C}}_{12n}^T\,\mathbf{a}_1 \\ &= \boldsymbol{C}_{12n}^T\,\mathbf{a}_2 - \tilde{\boldsymbol{C}}_{12n}^T\,\mathbf{a}_1 - B_{12n}, \end{aligned} \tag{23}$$

where $B_{12n} = \tilde{\chi}_{nz}^{\{1\}} - \chi_{nz}^{\{1\}} \in \mathbb{R}$.

With Eq. (23), the linearization of $\boldsymbol{D}(\boldsymbol{A}) = (..d_{ik}(\boldsymbol{q}_{kin}, \mathbf{a}_i, \mathbf{a}_k)..)^T \in \mathbb{R}^N$ around $\boldsymbol{A} = \mathbf{0}$ is given by

$$\boldsymbol{D}(\boldsymbol{A}) = \boldsymbol{Q}\boldsymbol{A} - \boldsymbol{B}, \tag{24}$$

where

$$\begin{array}{c} \begin{array}{ccccccccccc} & & \scriptstyle (k\text{-}1)\,7 & & \scriptstyle k\,7+1 & & \scriptstyle (i\text{-}1)\,7 & & \scriptstyle i\,7+1 & & \end{array} \\ \boldsymbol{Q} = \begin{pmatrix} & & \vdots & & \vdots & & \vdots & & \vdots & & \\ 0 & .. & 0 & \boldsymbol{C}_{ikn}^T & 0 & .. & 0 & -\tilde{\boldsymbol{C}}_{ikn}^T & 0 & .. & 0 \\ & & \vdots & & \vdots & & \vdots & & \vdots & & \end{pmatrix} \in \mathbb{R}^{N \times 7\,U}, \end{array} \tag{25}$$

and

$$\boldsymbol{B} = \begin{pmatrix} \vdots \\ B_{ikn} \\ \vdots \end{pmatrix} \in \mathbb{R}^N. \tag{26}$$

Funding. Christian Doppler Forschungsgesellschaft; Bundesministerium für Digitalisierung und Wirtschaftsstandort; Österreichische Nationalstiftung für Forschung, Technologie und Entwicklung; MICRO EPSILON MESSTECHNIK GmbH & Co. KG; ATENSOR Engineering and Technology Systems GmbH; TU Wien Bibliothek.

Acknowledgement. We thank Johannes Pfund and Ralf Dorn from Optocraft GmbH for their support and fruitful discussions.

Disclosures. The authors declare no conflicts of interest.

Data availability. Data underlying the results presented in this paper are not publicly available at this time but may be obtained from the authors upon reasonable request.

References

1. R. K. Tyson, *Adaptive optics engineering handbook* (Marcel Dekker New York, 2000).
2. J. Sheldakova, A. Kudryashov, V. Zavalova, and P. Romanov, "Shack-hartmann wavefront sensor versus fizeau interferometer for laser beam measurements," Proc. SPIE **7194**, 71940B (2009).
3. M. Rocktäschel and H. Tiziani, "Limitations of the shack–hartmann sensor for testing optical aspherics," Opt. Laser Technol. **34**(8), 631–637 (2002).
4. M. Fuerst, S. Unger, S. Ito, and G. Schitter, "Wavefront measurement based feedback control for automatic alignment of a high-na optical system," in *Journal of Physics: Conference Series*, vol. 1065 (IOP Publishing, 2018), p. 032001.
5. S. Chen, S. Xue, D. Zhai, and G. Tie, "Measurement of freeform optical surfaces: trade-off between accuracy and dynamic range," Laser Photonics Rev. **14**(5), 1900365 (2020).
6. D. R. Burada, K. K. Pant, M. Bichra, G. S. Khan, S. Sinzinger, and C. Shakher, "Experimental investigations on characterization of freeform wavefront using shack–hartmann sensor," Opt. Eng. **56**(8), 084107 (2017).
7. M. E. Fuerst and G. Schitter, "Scanning wavefront sensor for measurement of highly divergent wavefronts," IFAC-PapersOnLine **52**(15), 25–30 (2019).
8. M. E. Fuerst, E. Csencsics, N. Berlakovich, and G. Schitter, "Automated measurement of highly divergent optical wavefronts with a scanning shack–hartmann sensor," IEEE Trans. Instrum. Meas. **70**, 1–9 (2021).
9. K. K. Pant, D. R. Burada, A. Ghosh, G. S. Khan, and C. Shakher, "Improved subaperture stitching for the measurement of freeform wavefront," in *Laser Science*, (Optical Society of America, 2018), pp. JW4A–9.
10. K. K. Pant, D. R. Burada, M. Bichra, M. P. Singh, A. Ghosh, G. S. Khan, S. Sinzinger, and C. Shakher, "Subaperture stitching for measurement of freeform wavefront," Appl. Opt. **54**(34), 10022–10028 (2015).
11. K. K. Pant, D. R. Burada, M. Bichra, A. Ghosh, G. S. Khan, S. Sinzinger, and C. Shakher, "Weighted spline based integration for reconstruction of freeform wavefront," Appl. Opt. **57**(5), 1100–1109 (2018).
12. N. Berlakovich, M. E. Fuerst, E. Csencsics, and G. Schitter, "Robust wavefront segment registration based on a parallel approach," Appl. Opt. **60**(6), 1578–1586 (2021).
13. S. Chen, S. Li, and Y. Dai, "Iterative algorithm for subaperture stitching interferometry for general surfaces," J. Opt. Soc. Am. A **22**(9), 1929–1936 (2005).
14. N. Berlakovich, E. Csencsics, M. Fuerst, and G. Schitter, "Fast, precise, and shape-flexible registration of wavefronts," Appl. Opt. **60**(23), 6781–6790 (2021).
15. N. Berlakovich, E. Csencsics, M. Fuerst, and G. Schitter, "Iterative parallel registration of strongly misaligned wavefront segments," Opt. Express **29**(21), 33281–33296 (2021).

16. F. Fang, X. Zhang, A. Weckenmann, G. Zhang, and C. Evans, "Manufacturing and measurement of freeform optics," CIRP Ann. **62**(2), 823–846 (2013).
17. H. Tang, J.-A. Duan, S. Lan, and H. Shui, "A new geometric error modeling approach for multi-axis system based on stream of variation theory," Int. J. Mach. Tools Manuf. **92**, 41–51 (2015).
18. D. R. Neal, J. Copland, and D. A. Neal, "Shack-hartmann wavefront sensor precision and accuracy," in *Advanced Characterization Techniques for Optical, Semiconductor, and Data Storage Components*, vol. 4779 (International Society for Optics and Photonics, 2002), pp. 148–160.
19. W. H. Southwell, "Wave-front estimation from wave-front slope measurements," J. Opt. Soc. Am. **70**(8), 998–1006 (1980).
20. I. Mochi and K. A. Goldberg, "Modal wavefront reconstruction from its gradient," Appl. Opt. **54**(12), 3780–3785 (2015).
21. L. Huang, J. Xue, B. Gao, C. Zuo, and M. Idir, "Zonal wavefront reconstruction in quadrilateral geometry for phase measuring deflectometry," Appl. Opt. **56**(18), 5139–5144 (2017).
22. G. Zyskind and F. B. Martin, "On best linear estimation and general gauss-markov theorem in linear models with arbitrary nonnegative covariance structure," SIAM J. Appl. Math. **17**(6), 1190–1202 (1969).
23. F. P. León, *Messtechnik: Grundlagen, Methoden und Anwendungen* (Springer-Verlag, 2019).
24. Y. Chen and G. Medioni, "Object modelling by registration of multiple range images," Image Vis. Comput. **10**(3), 145–155 (1992).
25. L. Huang, J. Xue, B. Gao, C. Zuo, and M. Idir, "Spline based least squares integration for two-dimensional shape or wavefront reconstruction," Opt. Lasers Eng. **91**, 221–226 (2017).
26. H. Mao, Y. Liang, J. Liu, and Z. Huang, "A noise error estimation method for shack-hartmann wavefront sensor," Proc. SPIE **9678**, 967811 (2015).
27. A. Chernyshov, U. Sterr, F. Riehle, J. Helmcke, and J. Pfund, "Calibration of a shack–hartmann sensor for absolute measurements of wavefronts," Appl. Opt. **44**(30), 6419–6425 (2005).

Published version of the article: Nikolaus Berlakovich, Martin Fuerst, Ernst Csencsics, and Georg Schitter, "Improving the precision of parallel registration by incorporating a priori information," *Optics Express* Vol. 30, Issue 23, pp. 41473-41491, 2022. DOI: 10.1364/OE.469299